

# Axial Evolution of Helical Flame and Flow Disturbances in a Transversely Forced Combustor

Travis E. Smith,<sup>1</sup> Christopher M. Douglas<sup>2</sup>, Benjamin L. Emerson,<sup>3</sup> and Timothy C. Lieuwen<sup>4</sup>  
*Georgia Institute of Technology, Atlanta, GA, 30080*

This paper presents 5 kHz stereo PIV and OH PLIF measurements of transversely forced, triple nozzle swirl flames. This work is motivated by the problem of transverse instabilities in annular and can combustion systems. A key distinction of this problem from the axial instability problem is that the acoustic excitation field can differ substantially from one nozzle to the next; e.g., different nozzles can be located at either a pressure node or antinode in the case of a standing wave (where the pressure and transverse acoustic velocity field have an approximate 90 degree phase difference), or be excited by a traveling wave (where they are in phase). Prior modeling and experimental work has clearly shown that the dominant shear flow instabilities excited by these acoustics disturbances differ substantively as well. For example, axisymmetric jet modes are excited at pressure anti-nodes and helical modes at pressure nodes. These hydrodynamic disturbances then evolve axially at spatial growth rates controlled by the stability characteristics of the shear layer and nonlinear interactions with each other. This paper describes measurements in the  $r$ - $z$  and  $r$ - $\theta$  planes to characterize the axial evolution of these hydrodynamic disturbances excited by transverse acoustic waves. It shows that different helical modes, whose relative amplitudes near the nozzle outlet can be predicted in a straightforward way, evolve in quite different manners and are strongly influenced by not only the nature of the excitation field, but the nominal hydrodynamic stability characteristics of the swirling shear flow as well. These observations are compared with the results of a linear hydrodynamic stability analysis, demonstrating good qualitative agreement and supporting the idea that linear mechanisms, as opposed to nonlinear interactions, control which helical modes dominate the flow near the nozzle.

## Nomenclature

$\hat{B}_{j,m}$	= periodic azimuthal mode coefficient (index $j$ denotes $r$ , $z$ , or $\theta$ direction)
$\hat{B}_{ref,m}$	= periodic azimuthal mode coefficient predicted from forcing function
$\bar{B}_{j,m}$	= radially integrated magnitude of coefficient
$\bar{c}$	= flame progress variable contour
$D$	= nozzle outer diameter
$f_0, \omega_0$	= forcing frequency
$\bar{K}$	= integrated fluctuating kinetic energy
$k_i$	= imaginary part of wavenumber, spatial growth rate
$m$	= periodic azimuthal mode number
$\hat{R}_m$	= flame edge periodic azimuthal mode (non-dimensional)
$S_n$	= swirl number
$u_j$	= velocity component
$(\ )$	= frequency content of component
$r, z, \theta$	= cylindrical coordinate system
$x, y, z$	= Cartesian coordinate system

<sup>1</sup> Graduate Student, Aerospace Engineering, 635 Strong Street, Atlanta, GA 30318, AIAA Student Member.

<sup>2</sup> Graduate Student, Mechanical Engineering, 635 Strong Street, Atlanta, GA 30318, AIAA Student Member

<sup>3</sup> Research Engineer, Department Name, 635 Strong Street, Atlanta, GA 30318, AIAA Member.

<sup>4</sup> Professor, Aerospace Engineering, 270 Ferst Drive, Atlanta, GA 30332, AIAA Fellow.

## I. Introduction

THIS paper describes an analysis of the transversely forced shear layer dynamics of a combustng swirl flow. This work is motivated by the problem of transverse combustion instabilities, which pose significant operability challenges in premixed combustors [1, 2]. Previous work has been performed on both single nozzle and multi-nozzle experiments to study the swirling flow field and the effects of transverse and axial acoustic forcing [3-6]. O'Connor *et al.* recently reviewed transverse instabilities, and summarized key issues associated with transverse acoustic field structure, the excitation of hydrodynamic instabilities by transverse acoustic waves, and how the heat release responds to these disturbances [7]. A key feature of the transverse instability problem relative to the axial instability one is the fact that it generally introduces additional spatial degrees of freedom into the problem. For example, axial instabilities often can be approximated by a nominally one-dimensional acoustic field, and excite dominantly axisymmetric vortical structures that distort the flame in an axisymmetric manner. In contrast, transverse instabilities are associated with multi-dimensional acoustic fields and intrinsically three-dimensional, helical flow disturbances that subsequently disturb the flame. In addition, different nozzles/flames are located at different points in the traveling or standing wave structure in a transverse instability, and different hydrodynamic stability modes are excited at each location [8, 9].

In order to illustrate this point, decompose the velocity vector,  $u_j(r, \theta, z, t)$ , into frequency space and azimuthal disturbance modes, indexed by  $m$ :

$$\hat{u}'_j(r, \theta, z, \omega) = \sum_{m=-\infty}^{\infty} \hat{B}_{j,m}(r, z, \omega) e^{-im\theta} \quad (1)$$

where  $\hat{u}'_j$  is the Fourier transform of the fluctuating velocity field in the  $j$ -direction, and  $\hat{B}_{j,m}$  is the complex coefficient of the helical mode  $m$ . The  $m=0$  mode is axisymmetric while the  $m<0$  and the  $m>0$  modes denote co- and counter-swirling helical modes. In order to demonstrate how different helical modes were excited at different points in the standing wave structure, O'Connor *et al.* [7] expanded a transverse acoustic wave into these helical mode coefficients in an  $(r, \theta)$  coordinate system centered at a nozzle using the Jacobi-Anger expansion, i.e.,  $e^{ikx} = \sum_{m=-\infty}^{\infty} \hat{B}_{ref,m}(kr) e^{im\theta}$  (where  $x$  denotes the propagation direction of the transverse wave and  $k = \omega/c$  denotes the acoustic wave number). They showed that for a flame located at a pressure node/velocity antinode, that the acoustic disturbance excited odd hydrodynamic modes as  $\hat{B}_{ref,m} = i^{m-1} J_m(kr)$  (with the  $m=\pm 1$  modes being dominant), where  $r$  denotes the radial cylindrical coordinate; even modes are not excited. In contrast, even modes are excited as  $\hat{B}_{ref,m} = i^m J_m(kr)$  for a flame located at a pressure antinode (with the  $m=0$  mode being dominant); odd modes are not excited. Finally, for a traveling wave, both even and odd modes are excited as  $\hat{B}_{ref,m} = i^m J_m(kr)$ .

While this decomposition of the acoustic wave into nozzle-centered helical modes provides insight into how different hydrodynamic disturbances are excited by the acoustic field, it does not show these modes subsequently evolve. Rather, the axial evolution of these hydrodynamic disturbances is controlled by their spatial instability growth/decay rates, and also how these different disturbances may nonlinearly interact once they reach finite amplitude. Nonetheless, this expansion provides useful insight into several experimental studies. For example, the results of O'Connor *et al.* showed that when there is an acoustic pressure antinode at the nozzle, the  $m=0$  mode (manifested as an axisymmetric vortex) was the dominant mode of flow response, exciting axisymmetric flame wrinkling [7]. In contrast, when the transverse acoustic mode has a velocity antinode at the nozzle, the dominant response was an  $m=+1$  mode, with significant levels associated with the  $m=-1$  mode as well. Aguilar *et al.* [10] similarly studied a transversely forced configuration, comparing the response of a single and triple nozzle configuration. They similarly showed strong excitation of the  $m=0$  mode in both single and triple nozzle cases when the nozzle was located at the pressure anti-node, and the  $m=\pm 1$  mode when the nozzle was located at a pressure node. Work by Worth and Dawson [8] of self-excited transverse oscillations in an annular combustor showed that the heat release similarly depended on the position of the flame with respect to the acoustic wave. Similarly, Paschereit's groups observed that the flame response, as observed by OH\* chemiluminescence, was similar between traveling waves and when a pressure antinode is located at the nozzle [11, 12]. This observation is consistent with modeling results that suggest that the dominant flame response comes from the axisymmetric,  $m=0$  mode, which is excited for both traveling waves and pressure antinode cases [13].

Several important questions remain which are addressed in this study. First, while the initial excitation of the hydrodynamic modes by the acoustic field near the nozzle outlet appears well understood, the axial evolution of these disturbances in the presence of the flame requires further study. Clearly, the swirling, shear flows have their own preferentially excited disturbances, and so once these modes are excited, some will be preferentially amplified relative to others. These flows are also generally dispersive, and so the modes may also propagate at different phase speeds.

Also, while the above cited studies focused on the dominantly excited modes ( $m=0$  in one case,  $m=\pm 1$  in other), recent studies by Acharya *et al.* [13, 14] have shown that the global heat release response characteristics are intimately influenced by nonlinear triadic interactions between helical modes in cases where the nozzle is located at a pressure node. Further study is needed of the lower amplitude, even or odd modes that are also excited by transverse forcing. The objective of this paper is to address these questions, by describing measurements of the axial evolution of these fluid mechanic disturbances, as well as the flame dynamics.

## II. Facility and Flow Conditions

Figure 1a shows a schematic of the multinozzle combustor facility. It is similar to the facilities used by O'Connor *et al.* [15] and Aguilar *et al.* [10], with improved optical access, different nozzle configurations, and independent control of the nozzle flow rates and acoustic forcing. Two windows placed opposite each other allow optical access to the center nozzle and the interaction regions between nozzles. An additional window on top of the combustor above the center nozzle allows for a top-down view. Another optical port is placed on the side of the combustor to allow a laser sheet to bisect the combustor through the center of the nozzles.

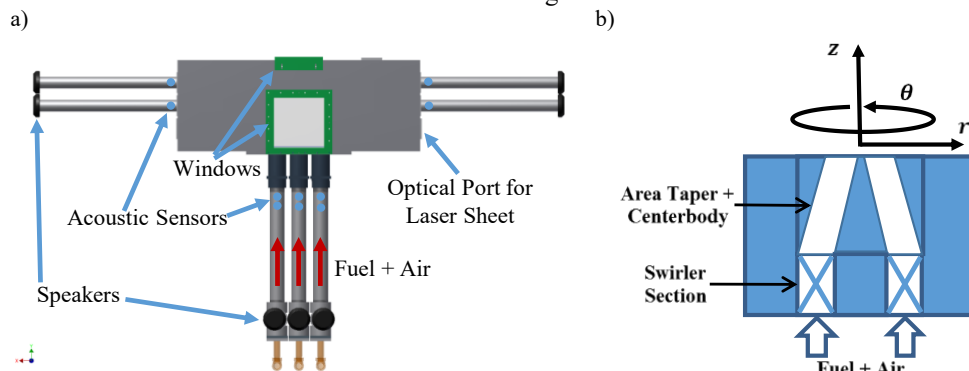


Figure 1. a) A schematic of the combustor and b) a schematic of the nozzle defining the coordinate system.

Also shown in Figure 1a are transverse acoustic forcing tubes with speakers attached to their ends. The magnitude of the signal to each speaker is the same, and the speakers on the left are either forced in phase (IP) or out-of-phase (OP) with the speakers on the right. This allows for the center nozzle to experience either a pressure antinode or a velocity antinode respectively, as verified previously [16]. Ten acoustic pressure sensors are placed in the system, 4 on the transverse acoustic tubes located 25.4 mm from the combustor and 6 on the premixing pipes located 203.2 mm from the nozzle exit and 25.4 mm apart. The combustor is forced transversely at a frequency of 390 Hz in both the IP and OP configurations. Figure 2 shows the spatially integrated power spectra (sum of the magnitude of each velocity component squared) defined in the region  $-0.75 < \frac{r}{D} < 0.75$  and  $0.1 < \frac{z}{D} < 1.2$ , taken in the  $r$ - $z$  plane. The calculation of the spectra at each point is explained later. The figure shows the clearly discernable forced peaks, as well as the order of magnitude larger energy in the velocity anti-node (OP) case, relative to the IP case.

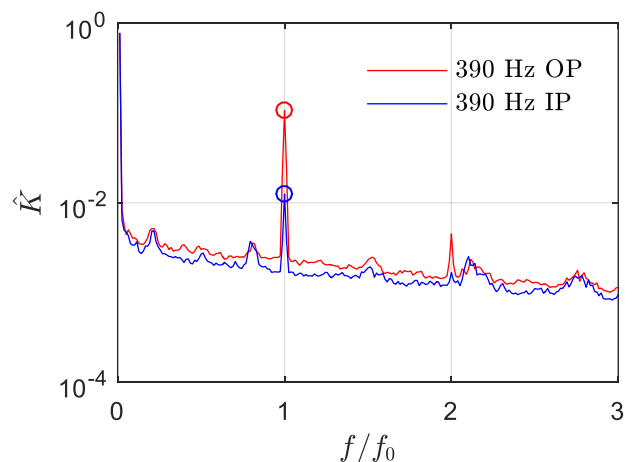


Figure 2. Spectra of the fluctuating kinetic energy for the acoustically forced cases calculated from the sPIV velocity fields.

The nozzle design is shown schematically in Figure 1b. An annular passage with inner and outer radii of  $r_{i,annulus}=18$  mm and  $r_{o,annulus}=31$  mm, respectively, is followed by an axial swirler with a geometric swirl of 0.6. The annular passage area then converges over an axial distance of 88.9 mm, to  $r_{o,nozzle}=18.4$  mm and  $r_{i,nozzle}=5$  mm, so that the annular area is reduced by 50%. The swirl number,  $S_n$ , of the flow calculated from a sPIV measurement is approximately 0.48, calculated as the ratio of the tangential to axial momentum and assuming constant density [17]

$$S_n = \frac{\int_0^{D/2} \bar{u}_\theta \bar{u}_z r^2 dr}{\frac{D}{2} \int_0^{D/2} \bar{u}_z^2 r dr} \quad (2)$$

The nozzles are spaced  $s/D=2.9$  apart. The three nozzles are each operated with a nozzle exit velocity of 25 m/s, as calculated from the air mass flow rate, with preheat temperature of 505 K at the nozzle exit. Fuel and air are premixed well upstream of the combustor to ensure thorough premixing and the center nozzle is operated at an equivalence ratio of  $\phi=0.95$ , and the outer nozzles at  $\phi=0.6$ . With this configuration, the center flame was stabilized in the inner shear layer (for this condition, it does not also attach in the outer shear layer, but exists as a v-flame), and acts as a “pilot” for the outer flames.

### III. Diagnostic Techniques

Simultaneous OH Planar Laser Induced Fluorescence (OH PLIF) and Stereoscopic Particle Image Velocimetry (sPIV) were taken at 5 kHz. A 527 nm double-pulsed laser, supplying 12 Watts per laser head, was used to place a 2mm thick laser sheet across the dump plane for sPIV. Two CMOS cameras were placed at equal angles to the plane containing the laser sheet and filtered to capture the scatter off of the 0.5-1 micron  $\text{TiO}_2$  particles. To measure the 25 m/s axial flow velocity, the PIV laser pulses were set 8 and  $14\mu\text{s}$  apart for  $r-\theta$  and  $r-z$  measurement orientations as explained later. A dye laser system tuned to a wavelength of 283.452 nm pumped by an Nd:YAG laser at 532nm was used for the OH PLIF. The OH fluorescence was captured using a CMOS camera coupled to a high speed intensifier. Three cylindrical mirrors were used on each of the lasers to condition the laser sheets before they are combined and passed into the combustor.

This paper considers two measurement planes: a horizontal plane parallel to the dump plane centered about the middle nozzle and a vertical plane passing through the centers of the three nozzles. These measurement planes are referred to as the  $r-\theta$  and  $r-z$  planes respectively. The  $r-\theta$  plane nomenclature is in reference to the cylindrical coordinate system defined by the nozzle geometry. For this plane, the laser sheet came through the window located on the side of the combustor with the two coplanar PIV cameras at 55 degrees from the normal of the laser sheet to capture forward and back scatter from the particles in the flow. The PLIF camera looked through a UV coated mirror through the top window. The laser sheet for the  $r-z$  plane came through the smaller side window of the combustor and was observed through the larger window by the three cameras with the sPIV cameras at an angle of 35 degrees from the normal. Measurements in the  $r-\theta$  planes were obtained at axial heights of  $z/D=0.15, 0.67, 1.2,$  and  $1.7$ . The jet merging occurs around  $z/D=2$ , so most of these measurement domains are upstream of the flow field and shear layer merging. Figure 3 shows the overlap of the calibrated PLIF and Mie scattering images for both the  $r-z$  and  $r-\theta$  measurement planes. These images show the location of the seeded reactant jet and inner shear layer stabilized flame. The uncertainty associated with the sPIV measurement is on the order of 1.5 m/s for in plane velocity components. The statistics presented below, however, have a much lower uncertainty due to the large sample size.

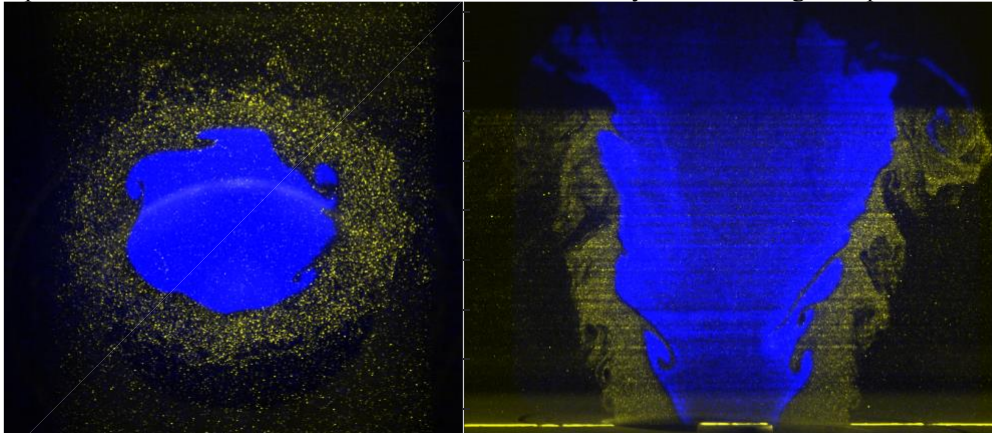


**Figure 3. Mie scattering (yellow) and OH-PLIF (blue) calibrated images overlaid for the a)  $r$ - $\theta$  unforced case and b)  $r$ - $z$  unforced case.**

#### IV. Post Processing Techniques

The two sets of image pairs acquired from the sPIV technique were processed using the Davis software from Lavision. This software calibrated all of the cameras and calculated the three-component velocity fields in Cartesian coordinates. For the purpose of calculating periodic azimuthal modes, the projection of helical modes onto the  $r$ - $\theta$  plane, the  $r$ - $\theta$  velocity vectors were interpolated onto a polar grid designed so that the radial spacing was roughly equal to the spacing in  $x$  and  $y$  of the original grid. The origin of the  $r$ - $\theta$  flow field was chosen as the point inside of the jet that maximizes the energy associated with an axisymmetric mode fit to the time-average velocity. The velocity components were then transformed into the cylindrical coordinate system shown in **Error! Reference source not found.**

A Fourier transform of the 7500 images was obtained at each point in the polar grid giving a frequency spectrum at each spatial location for each component of velocity. Each spectrum was estimated over a span of 0.2 seconds with a 75% overlap, resulting in 27 ensembles and giving a spectral resolution of 5 Hz. The ensembles were averaged to obtain the magnitude of the flow field, and a similarly averaged cross-power spectral density calculation was used to obtain the phase of the fluctuations. Eq. (3), seen below, shows the spatial decomposition of the frequency domain velocity measurements into periodic azimuthal modes.

$$\hat{B}_{j,m}(r, z, \omega) = \frac{1}{2\pi} \int_0^{2\pi} \hat{u}_j(r, \theta, z, \omega) e^{-im\theta} d\theta \quad (3)$$

In order to compare the relative strengths of the periodic azimuthal modes at each axial location, we radially integrate them following

$$\bar{B}_{j,m}(\omega, z) = \int_0^R |\hat{B}_{j,m}(\omega, z, r)| r dr, \quad (4)$$

where the outer limit of the integration  $R$  is the outer edge of the time-average outer shear layer, defined as

$$\frac{\partial (\hat{B}_{z,0}(R, \omega = 0))}{\partial r} \equiv 0.5 * \min \left( \frac{\partial (\hat{B}_{z,0}(r, \omega = 0))}{\partial r} \right). \quad (5)$$

$\bar{B}_{i,m}$  is the area weighted integral of the coefficient magnitudes from the centerline to the edge of the outer shear layer. Note that the choice of sign convention of the periodic azimuthal modes was set such that  $m < 0$  is counter-swirling, and  $m > 0$  is co-swirling.

Flame edges are extracted from the PLIF images by binarizing the field between zero (reactants) and unity (product). This digitized field is then averaged to create a progress variable field,  $\bar{c}$ . Additionally the flame edge is decomposed into periodic modes ( $\hat{R}_m$ ) using the same convolution equation.

#### V. Results and Analysis

Figure 4 plots a typical time averaged (top) and instantaneous (bottom) image of the flow field for the  $r$ - $\theta$  (left) and the  $r$ - $z$  (right) measurement planes. Overlaid on the time averaged figure are the  $\bar{c}=0.2$  and  $\bar{c}=0.8$  flame progress variable fields, shaded blue in-between them, and the axial velocity stagnation contour in black. Note that the color of the arrows in the time-averaged images quantify the out of plane velocity component.

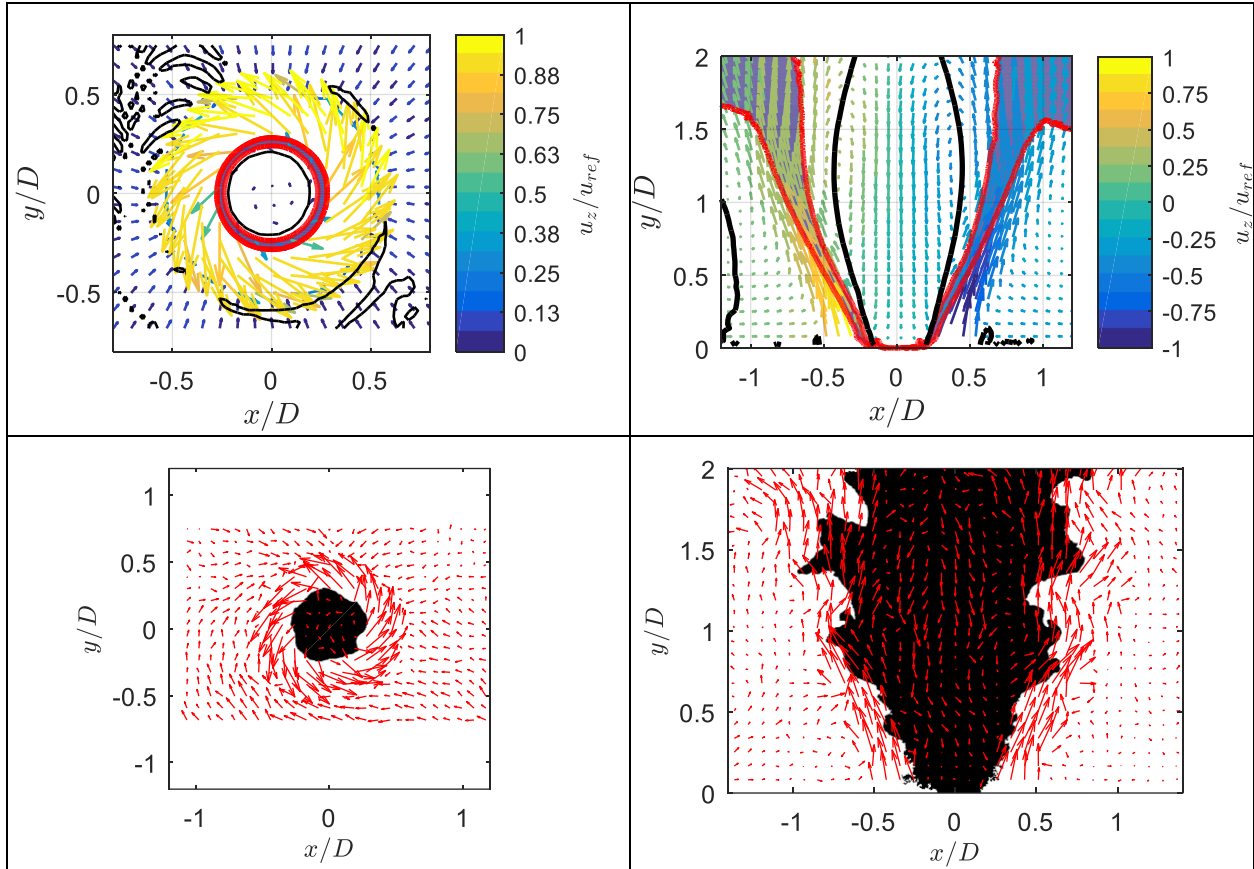
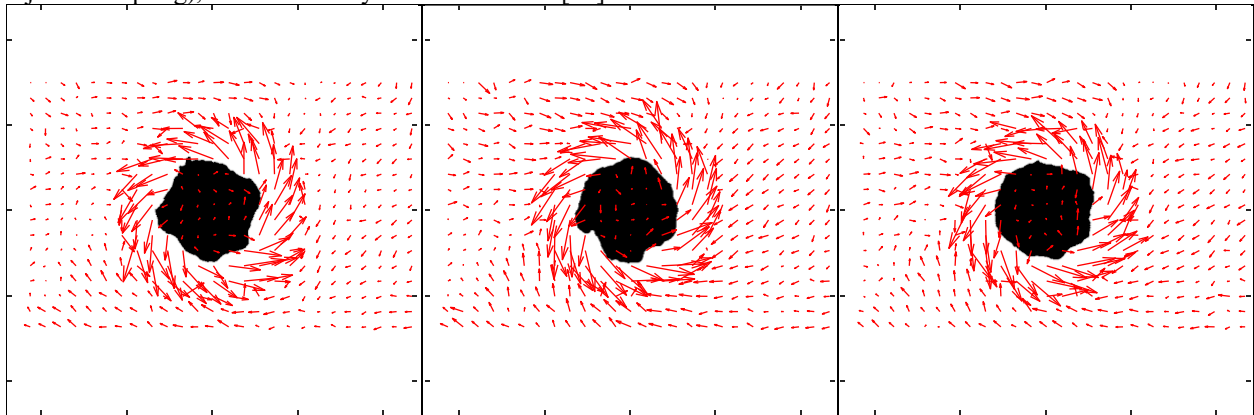
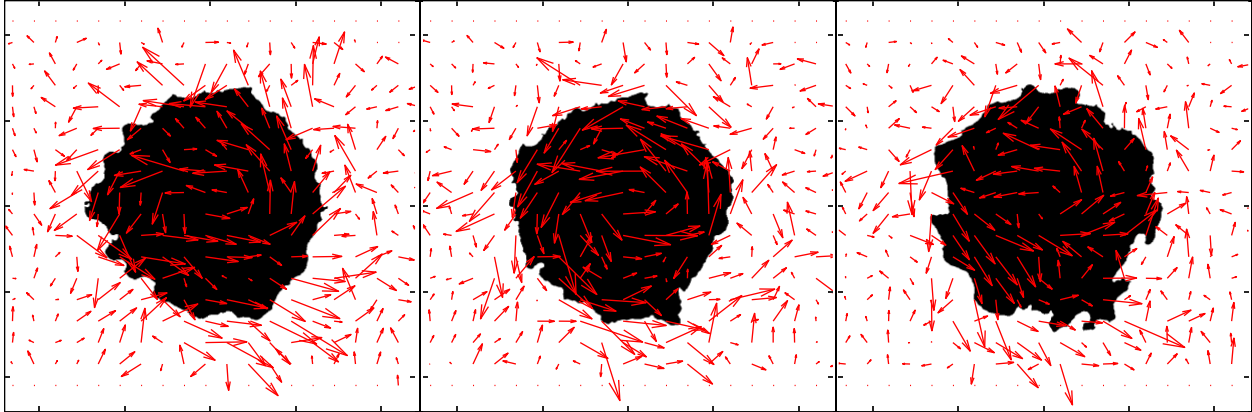


Figure 4. Sample time-averaged flow field with shaded blue area denoting flame brush ( $0.2 \leq \bar{c} \leq 0.8$ ) and axial stagnation overlay in red and black respectively (top) and sample instantaneous flow field overlaid on binarized and inverted PLIF image (bottom) for  $r-\theta$  at  $z/D=0.15$  (left) and  $r-z$  (right).

We next consider the IP forcing in more detail – this forcing configuration results in a symmetric pressure field across the nozzle, a pressure antinode, and strong axial forcing of the nozzle acoustics (sometimes referred to as injector coupling), as described by Blimbaum *et al.* [16].





**Figure 5** plots a series of instantaneous Mie and OH images at different axial locations. Note that the axisymmetric disturbance is weak near the nozzle exit and is not quite noticeable even at 1.2 diameters downstream. However, chemiluminescence measurements not shown in this paper suggest that this small disturbance is the leading contributor to spatially integrated heat release fluctuations. Figure 6 shows the azimuthal mode decomposition of two velocity components and the flame at a height of  $z/D=0.15$ . Shown for reference are the amplitude coefficients from the Jacobi-Anger decomposition of the model acoustic field distribution discussed in the introduction, where the function is integrated for values of  $r/D=0$  to 1, and  $k$  is calculated using  $c=453$  m/s and the forcing frequency. The data clearly shows the strong excitation of the  $m = 0$  mode, consistent with prior measurements and the predictions. The data also shows stronger magnitudes of the  $m=\pm 2$  modes relative to the reference line. This may be a reflection of the fact that these modes have had some spatial distance to develop or that there are distortions of the acoustic excitation field relative to the model one-dimensional field used for the decomposition. The other azimuthal modes are nonzero, presumably a manifestation of the turbulent fluctuations in the flow. Nonetheless, it is the strong  $m=0$  oscillations which lead to axisymmetric disturbances convecting downstream in the shear layers, similarly causing strong axisymmetric wrinkling of the flame.

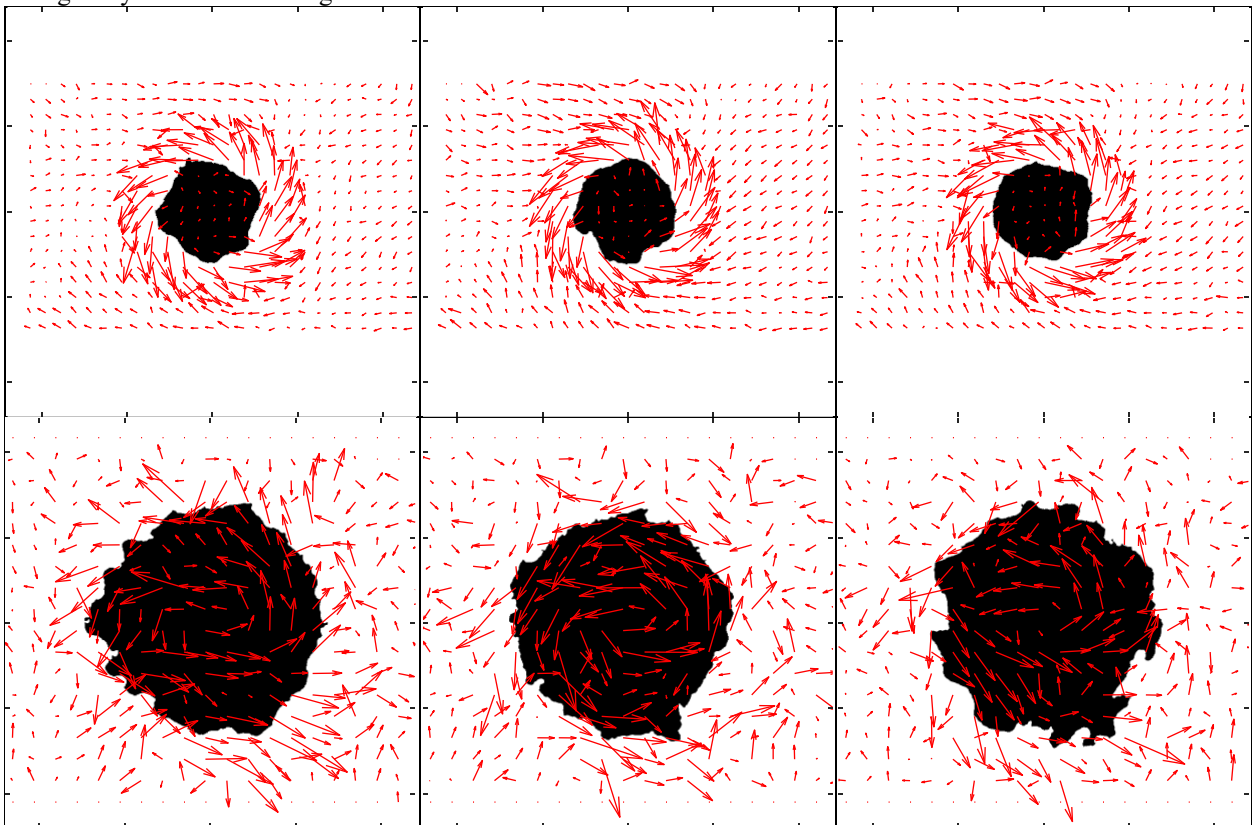


**Figure 5.** Sequential IP forcing images in  $r-\theta$  for  $z/D = 0.15$  (top) and 1.2 (bottom).

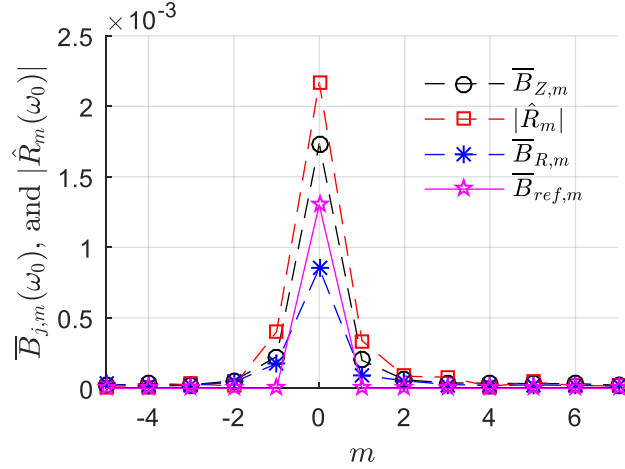


**Figure 6. Radially integrated helical mode coefficients of velocity fluctuations ( $\bar{B}_{j,m}$ ) for the 390 Hz IP forcing case ( $z/D=0.15$ ) and a scaled flame edge helical mode coefficient magnitude ( $\hat{R}_m$ ) compared to the scaled reference velocity function from the introduction integrated over the domain ( $\bar{B}_{ref,m} = \int_0^R |\hat{B}_{ref,m}| r dr$ ).**

Figure 7 plots corresponding images for the OP forcing case. In this case, a pressure node and a velocity antinode are nominally located at the centerline; i.e., the velocity is 180 degrees out of phase across the centerline. This results in a strong side-to-side flapping of the flame and flow field. At small axial distances, the disturbance is not very noticeable, however at larger distances, the disturbance can be clearly seen. The disturbance is shown here as a motion in the product region of the flame up over half a period of the forcing signal.

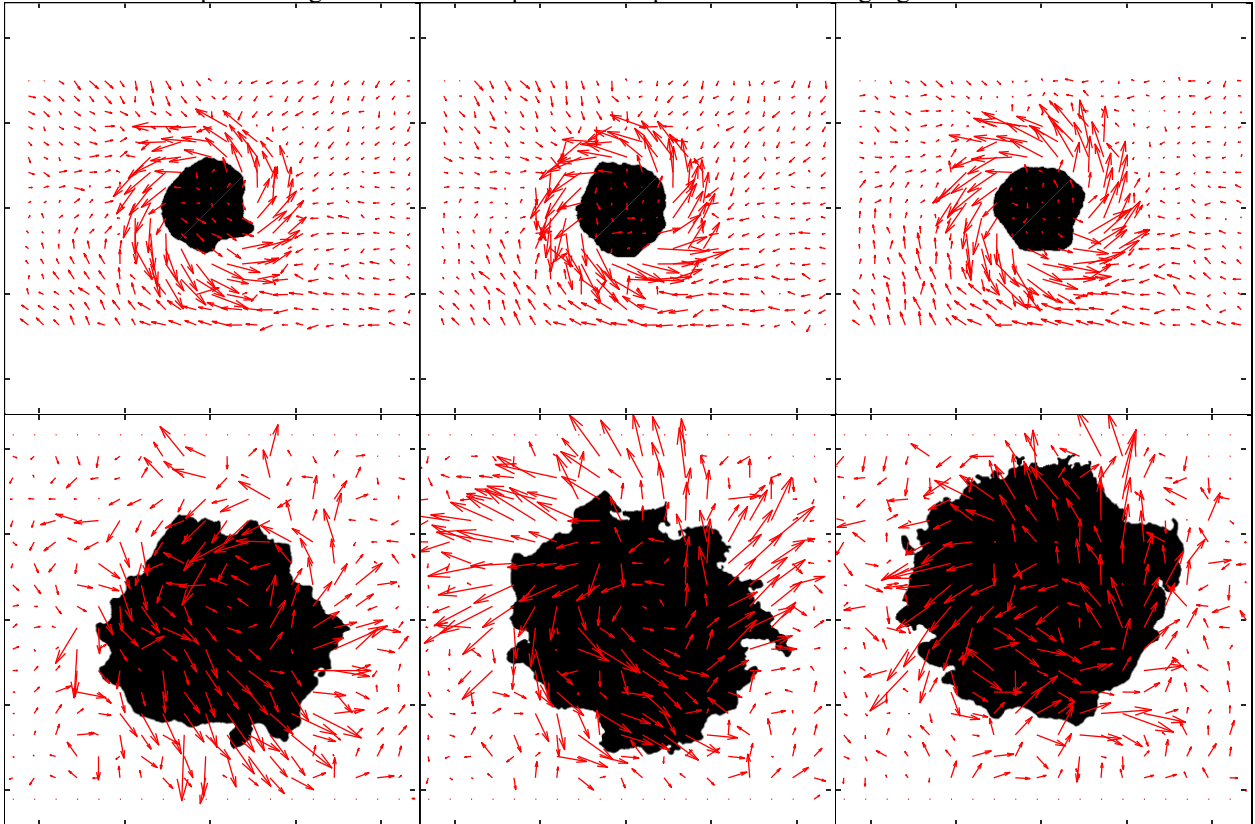


**Figure 7. Sequential OP forcing images in  $r-\theta$  for  $z/D = 0.15$  (top) and  $1.2$  (bottom).**

Figure 8 shows the azimuthal decomposition of the velocity field. Strong  $m=\pm 1$  modes are excited near the nozzle, consistent with prior observations [10] and model predictions. Also overlaid for reference are the model coefficients from the Jacobi-Anger expansion of the model velocity field. These helical disturbances manifest

themselves as staggered vortices and asymmetric flapping of the flame sheet. Note how the amplitude of the higher order helical disturbances,  $m=\pm 3$  are substantially larger than predicted by the model velocity field. Again, this is likely a manifestation of the fact that the data are taken at  $z/D=0.15$ , where they have had some time to spatially develop. In addition, note the small but nonzero  $m=0$  mode, due to some inherent axial motions induced at the nozzle exit.

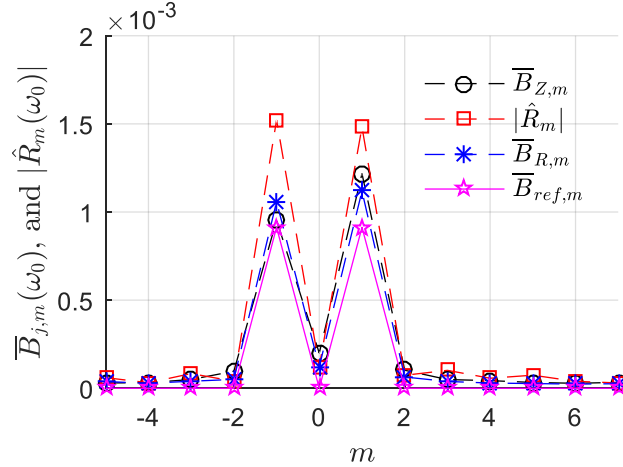


**Figure 8.** Radially integrated helical mode coefficients of velocity fluctuations ( $\bar{B}_{j,m}$ ) for the 390 Hz OP forcing case ( $z/D=0.15$ ) and a scaled flame edge helical mode coefficient magnitude ( $\hat{R}_m$ ) compared to the scaled reference velocity function from the introduction integrated over the domain ( $\bar{B}_{ref,m} = \int_0^R |\hat{B}_{ref,m}| r dr$ ).

Consider next the axial evolution of the dominant helical mode disturbances for the IP forcing case, plotted in Figure 9a. The figure shows that the  $m=0$  disturbance average remains the dominant disturbances as it is amplified as it convects downstream. Figure 9b shows the amplitude of the other helical modes, normalized by the  $m=0$  mode. It shows that the  $m=\pm 2$  modes also grow continuously with downstream distance, as it is similarly amplified spatially. Note also the growth of the  $m=+1$  mode. This mode is also the dominant one for the OP case, as discussed later; these behaviors may be evidence that the  $m=+1$  mode is the most amplified forced mode in the flow.

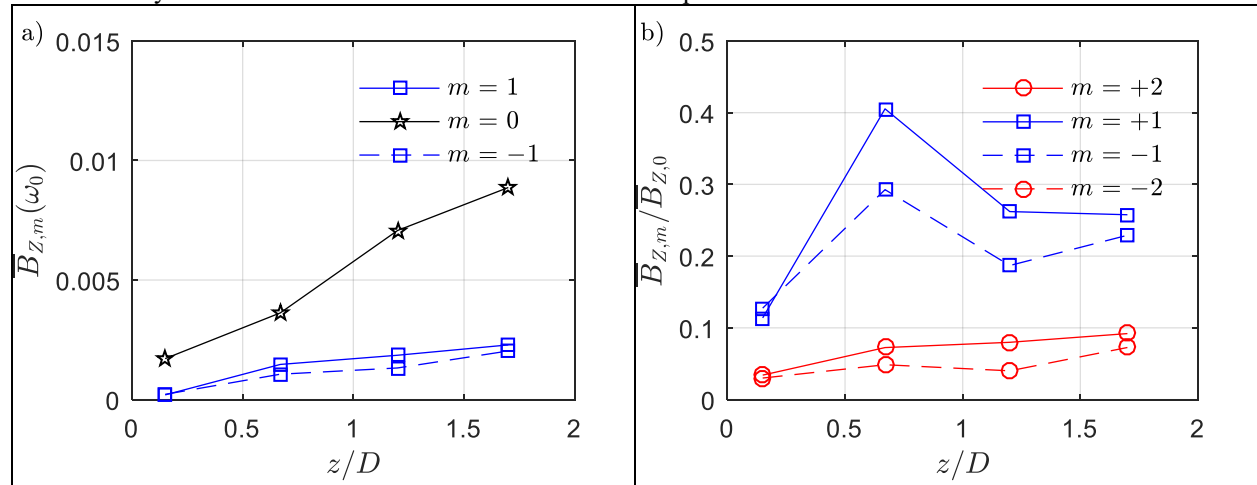


**Figure 9.** The 390 Hz IP a) radially integrated helical mode strength of the dominant axial velocity helical modes and b) ratio of radially integrated helical mode strength normalized by the  $m=0$  mode as a function of axial distance.

Figure 10a shows the corresponding plot for the OP forcing case. This figure clearly shows the preferential excitation of the  $m=+1$  mode relative to the  $m=-1$  mode. In other words, although the acoustic excitation excites both modes at the nozzle outlet equally, the natural flow instabilities amplifies the  $m=+1$  mode more strongly. Figure 10b also shows that the  $m=\pm 3$  are the most amplified of the other helical disturbances.

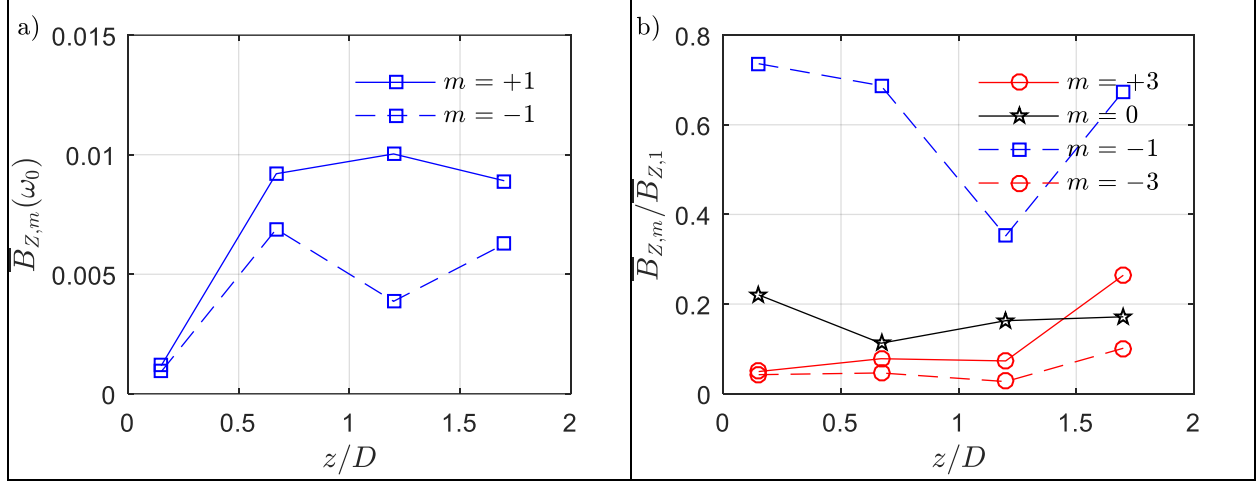


**Figure 10. The 390 Hz OP a) radially integrated helical mode strength of the dominant axial velocity helical modes and b) ratio of radially integrated helical mode strength normalized by the  $m=+1$  mode as a function of axial distance.**

Acharya *et al.* has shown that for nominally axisymmetric flames only the  $m=0$  mode excites heat release oscillations within the linear approximation [14]. However, nonlinear triadic interactions between  $m \neq 0$  modes can also lead to heat release oscillations, subject to the condition  $\sum_{k=1}^3 \alpha_k m_k = 0$  where  $m_k$  is the helical mode number and

$\alpha_k$  is an integer of 0, 1, or 2 and satisfies the condition  $\sum_{k=1}^3 \alpha_k = 3$ . For example, the relative amplitudes of the  $m=$

3, +2, and +1, or the  $m=+3, -2,$  and  $-1$  modes have particular dynamical significance in terms of the heat release oscillations which they excite.

To determine whether the preferential excitation of the co-swirling modes is a linear phenomenon or a manifestation of nonlinear interactions between modes, a linear hydrodynamic spatial (local) stability analysis was performed on the velocity and density data from the unforced time-averaged flowfield using tools that are previously described elsewhere [18]. This spatial stability analysis predicts the spatial growth rate  $-k_i$  for a disturbance at a given excitation frequency. The stability analysis indicated that the most unstable  $m=+1$  (co-swirling) mode behaves as an amplifier while the most unstable  $m=-1$  (counter-swirling) mode behaves as an oscillator. This result is common among the swirling flow literature [19] and may be attributed to greater relative shear associated with counter-swirling helices compared to axisymmetric rings or co-swirling helices [20].

The frequency of the self-excited behavior of the counter-swirling  $m=-1$  mode remains below 200 Hz throughout the domain. At the forcing frequency of 390 Hz, both of the  $m=\pm 1$  modes behave as amplifiers, and, as a result, we have restricted our analysis to a spatial analysis at the forcing frequency alone. Figure 11a shows the spatial growth rate ( $-k_i$ ) of the most-unstable  $m=\pm 1$  modes as a function of downstream distance at 390 Hz. This figure indicates that the linear hydrodynamics predict that the  $m=+1$  mode is amplified more strongly and for a larger part of the domain than its  $m=-1$  counterpart which agrees with the trend seen in the experiment.

Figure 11b shows the evolution of the relative disturbance amplitude, calculated using the WKB method shown in Equation 6, for both of the most-unstable  $m=\pm 1$  modes as a function of axial distance at 390 Hz.

$$\frac{|\hat{u}'_z(\omega_0)|}{|\hat{u}'_{z,0}(\omega_0)|} = e^{\int_{z_0}^z -k_i dz'} \quad (6)$$

The predicted growth rates are in qualitative agreement with the experimental results. Some key features of the envelope are successfully predicted, namely (1) the relative dominance of the  $m=+1$  mode, (2) the axial location of the peak perturbation amplitudes, denoting the change from amplification to damping, and (3) the axial extent over which the envelope is initially amplified. This result suggests that the experimentally observed dominance of the  $m=+1$  mode over the  $m=-1$  mode is a manifestation of linear processes, and not a nonlinear interaction between the two modes.

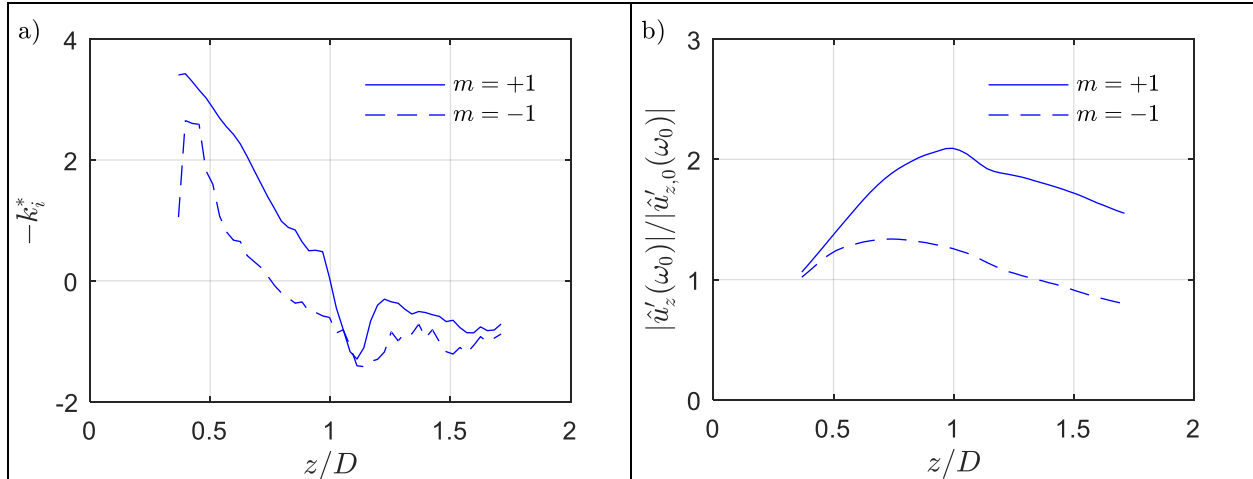


**Figure 11. Results from spatial stability analysis showing the predicted a) spatial growth rate at 390 Hz as a function of distance for  $m=\pm 1$  and b) normalized perturbation amplitude at 390 Hz as a function of distance for  $m=\pm 1$ .**

One aspect of the experiment which this hydrodynamic analysis did not qualitatively match was the observed secondary growth of the  $m=-1$  mode between  $1.2 < z/D < 1.7$  (see Figure 10), after an initial growth and decay interval. This particular phenomenon and the spatial distribution of the disturbances will be considered more deeply in future work by the authors.

## VI. Conclusion

This paper has shown how flow field helical modes, excited by transverse forcing, evolve axially in the presence of the flame. Acoustically forced measurements showed that the dominant helical modes could be qualitatively predicted with forcing function expressions derived by O'Connor *et al.* [7]. However, these modes can evolve axially in a quite different manner, particularly for the OP forcing case where  $m=+1$  grows much more rapidly than the  $m=-1$  mode, although both start with similar magnitudes. Because theoretical analysis has suggested that nonlinear interactions between different helical modes have important influences on heat release oscillations, we also show how other helical modes evolve, such as  $m=\pm 2$  or  $\pm 3$  modes. While these modes have low amplitudes relative to the dominant modes, they have their largest amplitudes downstream where the flame area is the largest (the flame is a v-flame, whose surface area grows monotonically with downstream distance as it spreads radially), and so their importance cannot be dismissed outright.

A linear stability analysis result was also presented to shed more light on why the  $m=+1$  and  $m=-1$  modes grow at different rates. It was found that the  $m=+1$  mode had a larger spatial growth rate for a longer spatial distance than the  $m=-1$  mode at the forcing frequency. The predicted growth rates from the stability analysis were compared with the observed trends. It was found that there was good qualitative agreement between the experiment and the prediction in that the relative mode dominance, peak location, and growth trends matched. This suggests that the dominant mechanism in the growth of the two modes is linear.

## Acknowledgments

This research was partially supported by funding from Pratt & Whitney. Additionally the authors would like to thank Jamie Lim and Aaron Prakash Naidu for their aid in the experimental aspect of this paper.

## References

- [1] Lieuwen, T., and Yang, V. *Combustion Instabilities in Gas Turbine Engines: Operational Experience, Fundamental Mechanism and Modeling*. Washington D.C: AIAA, 2005.
- [2] Lieuwen, T. *Unsteady Combustor Physics*: Cambridge University Press, 2012.
- [3] Schwing, J., Sattelmayer, T., and Noiray, N. "Interaction of Vortex Shedding and Transverse High-Frequency Pressure Oscillations in a Tubular Combustion Chamber," *ASME Turbo Expo*. Vancouver, Canada, 2011.

- [4] Rosa, A. J. D., Samarasinghe, J., Peluso, S. J., Quay, B. D., and Santavicca, D. A. "Flame Area Fluctuation Measurements in Velocity-Forced Premixed Gas Turbine Flames," *Journal of Engineering for Gas Turbines and Power* Vol. 138.4, 2016.
- [5] Steinberg, A. M., Arndt, C. M., and Meier, W. "Parametric study of vortex structures and their dynamics in swirl-stabilized combustion," *Proceedings of the Combustion Institute*. Vol. 34, 2013, pp. 3117-3125.
- [6] Bourgooin, J. F., Durox, D., Moeck, J. P., Schuller, T., and Candel, S. "A new pattern of instability observed in an annular combustor: The slanted mode," *Proceedings of the Combustion Institute*. Vol. 35, 2015, pp. 3237-3244.
- [7] O'Connor, J., Acharya, V., and Lieuwen, T. "Transverse Combustion Instabilities: Acoustics, Hydrodynamics, and Flame Dynamics," *Progress in Energy and Combustion Sciences*. 2015.
- [8] Worth, N. A., and Dawson, J. R. "Self-excited circumferential instabilities in a model annular gas turbine combustor: Global flame dynamics," *Proceedings of the Combustion Institute*. Vol. 34, 2013, pp. 3127-3134.
- [9] Worth, N. A., and Dawson, J. R. "Modal dynamics of self-excited azimuthal instabilities in an annular combustion chamber," *Combustion and Flame* Vol. 160, No. 11, 2013, pp. 2476-2489. doi: 10.1016/j.combustflame.2013.04.031
- [10] Aguilar, M., Malanoski, M., Adhitya, G., Emerson, B., Acharya, V., Noble, D., and Lieuwen, T. "Helical Flow Disturbances in a Multinozzle Combustor," *Journal of Engineering for Gas Turbines and Power-Transactions of the Asme* Vol. 137, No. 9, 2015. doi: Artn 091507 10.1115/1.4029696
- [11] Saurabh, A., and Paschereit, C. O. "Combustion Instability in a Swirl Flow Combustor with Transverse Extensions," *Proceedings of the Asme Turbo Expo: Turbine Technical Conference and Exposition, 2013, Vol 1b*. 2013.
- [12] Saurabh, A., Steinert, R., Moeck, J. P., and Paschereit, C. O. "Swirl Flame Response to Traveling Acoustic Waves," *Proceedings of the Asme Turbo Expo: Turbine Technical Conference and Exposition, 2014, Vol 4b*. 2014.
- [13] Acharya, V. S., Shin, D. H., and Lieuwen, T. "Premixed Flames Excited by Helical Disturbances: Flame Wrinkling and Heat Release Oscillations," *Journal of Propulsion and Power* Vol. 29, No. 6, 2013, pp. 1282-1291. doi: 10.2514/1.B34883
- [14] Acharya, V., and Lieuwen, T. "Premixed Flame Response to Helical Flow Disturbances: Non-linear Effects," *9th U. S. National Combustion Meeting*. 2015.
- [15] O'Connor, J., and Lieuwen, T. "Disturbance Field Characteristics of a Transversely Excited Burner," *Combustion Science and Technology* Vol. 183, No. 5, 2011, pp. 427-443.
- [16] Blimbaum, J., Zanchetta, M., Akin, T., Acharya, V., O'Connor, J., Noble, D. R., and Lieuwen, T. "Transverse to longitudinal acoustic coupling processes in annular combustion chambers," *International Journal of Spray and Combustion Dynamics* Vol. 4, No. 4, 2012, pp. 275-297.
- [17] Gupta, A. K., Lilley, D. G., and Syred, N. *Swirl Flows*: Abacus Press, 1984.
- [18] Emerson, B., and Lieuwen, T. "Dynamics of harmonically excited, reacting bluff body wakes near the global hydrodynamic stability boundary," *Journal of Fluid Mechanics* Vol. 779, 2015, pp. 716-750. doi: 10.1017/jfm.2015.450
- [19] Loiseleux, T., Chomaz, J. M., and Huerre, P. "The effect of swirl on jets and wakes: Linear instability of the Rankine vortex with axial flow," *Physics of Fluids* Vol. 10, No. 5, 1998, p. 1120. doi: 10.1063/1.869637
- [20] Oberleithner, K., Paschereit, C. O., and Wygnanski, I. "On the impact of swirl on the growth of coherent structures," *Journal of Fluid Mechanics* Vol. 741, 2014, pp. 156-199. doi: 10.1017/jfm.2013.669